Automatic Stent Implant Follow-up in Intravascular Optical Coherence Tomography Images

Serhan Gurmeric[1], Gozde Unal[1], Stephane Carlier[2], Yan Yang[3], and Greg Slabaugh[3]

[1] Faculty of Engineering and Natural Sciences, Sabanci University, Turkey
{sgurmeric,gozdeunal}@sabanciuniv.edu,
[2] Cordis Corporation J&J, Belgium,
[3] Siemens Corporate Research, Princeton, NJ USA

Abstract. Atherosclerotic plaques and their rupture cause narrowing or blockage of the coronary arteries and may lead to sudden cardiac death. As a remedy, after a coronary angioplasty, often a stent is implanted to prevent restenosis. Although it was observed that drug-eluting stents can significantly reduce the occurrence of neointimal hyperplasia, in-stent restenosis still occurs, therefore, studying the distribution of the stent struts during patient follow-ups is important. In this paper, we will present new computer methods for automated analysis of strut distribution in monitoring the restenosis and degree of neointimal tissue growth over struts from the intravascular optical coherence tomography data. Our system will be a useful computer-aided monitoring tool for follow-up studies of stent implantation in the clinical workflow.

1 Introduction

Coronary artery diseases such as atherosclerosis are the leading cause of death in the industrialized world. Medical imaging techniques have greatly assisted the diagnoses and treatments for coronary artery diseases. These imaging approaches include coronary X-ray angiography, computed tomography angiography (CTA), magnetic resonance angiography (MRA), intravascular ultrasound (IVUS), and optical coherence tomography (OCT). Among them, CTA and MRA are non-invasive imaging modalities, but the low resolution has limited their ability to resolve different constituents of atherosclerotic plaques. IVUS and intravascular OCT, however, are able to achieve much higher resolution than CTA and MRA by performing invasive catheterization on patients. OCT is a relatively new imaging technique that is analogous to ultrasound, but it measures the intensity of back-reflected infrared light instead of acoustical waves [1]. OCT has shown promise as a method for intravascular imaging, and was compared to IVUS in several works [2, 3]. The biggest advantage of OCT is its high resolution. Both in vitro and in vivo studies [2, 4] have shown that the resolution (on the order of 10 μm) can not only differentiate between typical constituents of atherosclerotic plaques, such as lipid, calcium, and fibrous tissue, but can also resolve the thin fibrous cap that is thought to be responsible for plaque vulnerability[5]. Atherosclerotic plaques may cause narrowing or blockage of the coronary arteries, resulting in reduced blood supply to the heart tissue, and sometimes lead to serious results such as heart attacks. To open a blockage, the procedure of percutaneous transluminal coronary angioplasty (PTCA) is usually applied, and a stent is often implanted after angioplasty to keep the artery open and prevent restenosis (regrowth of the plaque). Stents are small metal scaffolds either made from bare metal or coated with drug to inhibit restenosis. The

former are known as bare-metal stent (BMS) and the latter are known as drug eluting stents (DES). It was observed that drug-eluting stents can significantly reduce the occurrence of neointimal hyperplasia (NIH) [6]. However, in-stent restenosis after drug-eluting stents implantation still occurs[7]. Studies have shown that nonuniform circumferential stent strut distribution affects local drug concentration [8], thus the number and distribution of the stent struts might also affect the magnitude of NIH after stent implantation in human coronary arteries [9]. Therefore, automatic computer methods for analysis of strut distribution in monitoring the restenosis and degree of neointimal tissue growth over struts will help the clinical workflow and increase efficiency of stent implant follow-ups.

Previous studies on stent strut distribution, mentioned above, performed manual detection and measurement of the stent struts, and require enormous amount of time to process OCT pullbacks. An automatic stent detection method in [10] was developed by using brightness pattern in IVUS images. In this paper, we present a novel automated method for analysis of strut distribution during stent implant follow-up in patients from the OCT pullback datasets, which exhibit different characteristics than IVUS data. We developed a new spline contour evolution for delineating both the lumen boundary and the struts in the case of neointimal hyperplasia. We then describe an algorithm for detecting stent struts in a series of OCT images. In our developed computer application, for clinical use purposes, we also incorporated interactive features for correcting the splines and marking struts if necessary. Section 2 explains the steps and details of our algorithm, Section 3 presents the validation results and experiments, and Section 4 concludes with discussions.

2 Method

In this section, we explain our method for stent detection and analysis in OCT pullbacks. The raw image data format is in the rectangular domain as shown in Figure 1.a, and we developed our method completely using the native image data rather than the scan-converted polar image in Figure 1.b.[4]

2.1 Preprocessing the OCT pullbacks

Catheter artifacts, which form ring-like shadows around the catheter center in the image interferes with the image processing operations such as computation of image gradients, therefore, a prefiltering of the image is usually required.

We observe that in OCT pullbacks, the arterial wall and stent struts fall into the brighter intensity range, which hence contains the useful target information for our purposes. As a preprocessing step, we carry out a histogram based filtering approach to exploit this character of the OCT image. The density for image intensities, call $p(i)$, is estimated through a histogram, and typically, a unimodal distribution with a heavy tail towards the bright intensity side is obtained (Figure 1.c). The most likely value of $p(i)$, i.e. its mode, is computed. To eliminate the noise from the lower intensities, and concentrate on the brighter side of the density values on the right side of the mode, a certain percentage, say b, of the mode is computed, and all those intensities below that value is annihilated to 0 (Figure 1.f). After this step, a Gaussian filter with a variance of $\sigma = 2.5$ was applied and a morphological opening operation was performed to remove the remaining isolated bright pixels in dark

[4] Note that in the intravascular image processing community, the terms polar and rectangular image are used interchangeably. We call the display image (circular) as the polar image and the raw image as the rectangular image as recommended by the cardiologist imaging expert in the team.

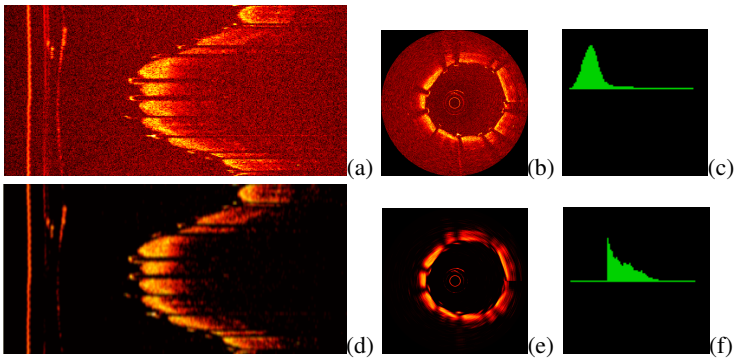

Fig. 1. (a) raw image (rectangular domain); (b) display image (polar domain); (c) Density estimate of the image (a); (d) rectangular image after filtering (a); (e) display image of (d); (f) Density estimate of the image (d).

regions. The result of the overall pre-filtering operation is shown in Figure 1.d-e. The pre-filtered image will be utilized next in the spline contour propagation step, which will be followed by the strut detection.

2.2 Spline Segmentation for Lumen and Stent

The lumen boundary is represented by a deformable spline contour and will be propagated with ordinary differential equations, which will be derived for its evolution. Deformable models or active contours [11] have proven to be versatile models in segmentation of various anatomic structures such as vessel borders [12].

First, as required in most active contour methods, a good initialization is preferable for the success of the active contour method. For that purpose, we will detect the arterial wall that appears as a wide bright 1-dimensional (1D) blob from the near field towards the far field of the catheter.

Spline Initialization: We developed an algorithm for initializing our spline control points on a pullback image frame as follows:

1. Shoot rays from the center of the image, i.e. take a row, say row y, of the rectangular image, apply a closing operation (dilate and erode) to smooth and fill small gaps in order for the 1D signal $I(x)$ where $x \in [0, N]$ to become differentiable. This operation is done on every other k^{th} row (e.g. 6^{th}) to initialize a certain variable number of control points of the spline so that enough variability of the lumen contour will be captured.
2. Detect the following over each 1D signal:

$$(I(x_1) = 0) \,\&\, \left(\frac{dI(x_1)}{dx} > 0\right) \tag{1}$$

then

$$\left(\frac{dI(x_2)}{dx} < 0\right) \,\&\, (I(x_2 + 1) = 0) \tag{2}$$

These rules lead to detection of the bright intensity peaks.

3. Over the detected intervals $h = x_2 - x_1$, find the maximum width h.
4. If $h <$ "minimum width threshold", go to the next selected row signal, i.e. go to step 1.
5. If a maximum h is found, detect the beginning of that interval, i.e. x_1. Record x_1 as the control point.
6. Repeat 1-5 until all rows of the rectangular image is processed.
7. The spline now can be initialized at the control point set (x_1, y) collected via the above algorithm.

Spline Evolution: We utilized a cubic spline, with four polynomial blending functions. The initial spline obtained from our method above is usually very close to the lumen border, and is only supposed to evolve a few pixels for a refinement. We utilize a geodesic active contour energy functional [13, 14]:

$$E(\boldsymbol{C}) = w_1 \cdot \text{image term} + w_2 \cdot \text{smoothness term} = w_1 \int_{\boldsymbol{C}} F ds + w_2 \int_{\boldsymbol{C}} ds \quad (3)$$

where w_1, w_2 are the weights of the data term and the smoothness term on the contour, and $F = g(|\nabla I|)$, where g is a monotonically decreasing function inversely proportional to the image gradient: $g = 1/(1 + |\nabla I|)$.

In an earlier similar spline-based active contour work [15], uniform rational B-splines [16] were utilized. Here, the lumen contour is represented with a Catmull-Rom spline, which belong to a family of cubic interpolating splines, [17] with four cubic polynomials functions: $h_{00}(t) = 2t^3 - 3t^2 + 1$, $h_{10}(t) = t^3 - 2t^2 + t$, $h_{01}(t) = -2t^3 + 3t^2$, and $h_{11}(t) = t^3 - t^2$, where $t \in (0, 1)$ for each interval, i.e. between two control points. One difference of Catmull-Rom splines from B-splines is that the interpolated contour goes exactly through the control points since the segments are formed using the two end points $\boldsymbol{P}_j$ and $\boldsymbol{P}_{j+1}$ and their tangents $\boldsymbol{T}_j$ and $\boldsymbol{T}_{j+1}$:

$$\boldsymbol{C}_j(t) = h_{00}(t)\boldsymbol{P}_j + h_{01}(t)\boldsymbol{P}_{j+1} + h_{10}(t)\boldsymbol{T}_j + h_{11}(t)\boldsymbol{T}_{j+1}, \;\; j = 1...K \quad (4)$$

The contour $\boldsymbol{C}$ will be a concatenation of the segments $\boldsymbol{C}_j$. Note that the control points $\boldsymbol{P}_j$ and segments $\boldsymbol{C}_j$ have the same index for a clockwise transversal of the spline, and very close control points will be deleted for regularity of the contour. The tangent vectors are formed by the simple three point differences:

$$\boldsymbol{T}_j = \frac{(\boldsymbol{P}_{j+1} - \boldsymbol{P}_j) * 0.5}{|(\boldsymbol{P}_{j+1} - \boldsymbol{P}_j)|} + \frac{(\boldsymbol{P}_j - \boldsymbol{P}_{j-1}) * 0.5}{|(\boldsymbol{P}_j - \boldsymbol{P}_{j-1})|} \quad (5)$$

for internal points $j = 2, ..., K - 1$, and one-sided differences are used at the endpoints of the control point set. One nice property of the Catmull-Rom spline is its practicality for interaction purposes because when the user clicks to draw or correct spline points, the constructed contour goes through the exact points, which the user marks.

We propose a new modified spline evolution, in which the control points of the spline will be evolved by integrating image energy terms from its two adjacent segments. The differential equation for the control points, i.e. the motion equation of the spline, are thus obtained as:

$$\frac{\partial \boldsymbol{P}_j}{\partial t} = \int_{\boldsymbol{C}_j} (w_1 F\kappa + w_2\kappa)\, \boldsymbol{N}_j ds + \int_{\boldsymbol{C}_{j-1}} (w_1 F\kappa + w_2\kappa)\, \boldsymbol{N}_{j-1} ds - w_1 \left(\int_{\boldsymbol{C}_j} \boldsymbol{\nabla} F_n + \int_{\boldsymbol{C}_{j-1}} \boldsymbol{\nabla} F_n \right) \quad (6)$$

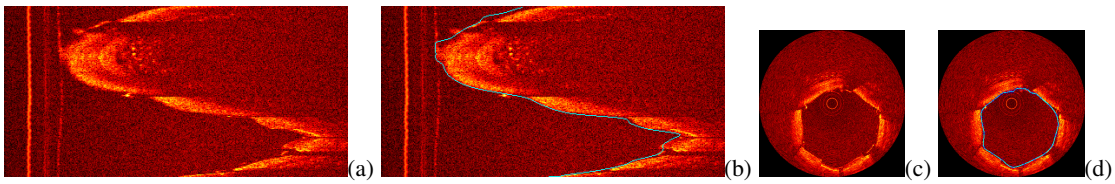

Fig. 2. (a) and (c) OCT images without splines; (b) and (d) with splines deformed to fit to the lumen border.

where κ is the curvature on the spline segment, and $\boldsymbol{N}_j$ is the unit normal vector over the segment $\boldsymbol{C}_j$, which is the next segment and $\boldsymbol{C}_{j-1}$ is the previous segment for the control point $\boldsymbol{P}_j$. The last two terms include the normal component: $\boldsymbol{\nabla} F_n = (\boldsymbol{\nabla} F \cdot \boldsymbol{N})\boldsymbol{N}$. Geodesic active contours have a well-known drawback as being too local during contour evolution since they depend on pointwise image gradients. With Eq (6), this problem is alleviated by the both the semi-globalization and the smoothing effect provided by integration of the image terms on two adjacent spline segments of the current control point.

In summary, Eq (6) updates the control points $\boldsymbol{P}_j$, and hence the contour $\boldsymbol{C}$ is updated to deform towards the lumen border in a smooth geometry as shown in sample results in Figure 2.

Three situations require attention during processing OCT pullbacks for stent implant follow-up: newly implanted stent case; minimum neointimal hyperplasia case such as a follow-up of a DES; and more important NIH or instent restenosis cases, which all present different challenges to the algorithm.

Newly Implanted Stent case: This is the situation with a stent freshly implanted into the artery, hence the vessel wall tissue did not have the chance to grow over the struts yet. The struts shadows are usually visible as in Figure 2. The first spline contour estimated using the update equation Eq (6) is used in strut detection which will be explained in the next section.

Minimum and Important Neointimal Hyperplasia Cases: In the follow-up studies of stent implantation, the stent struts are usually not directly in contact with the blood pool. Instead, there is an extra layer of neointimal hyperplasia (NIH). Figure 3 depicts a case with minimal NIH development (a) and a case with more prolific development of NIH (c). For a strut detection using our method (next subsection) on the images with NIH, the results would not be satisfying because the lumen spline segmentation result is far away from the actual stent boundary. The spline contour estimated using the update equation Eq (6) is used as the first spline, and a second one is initialized as a dilated version of the first one over the artery wall. Then, Eq (6) is used for the second spline as well over smoothed image intensities. This second spline then gets stuck at the bright strut edges, and will be used in the strut detection that will be explained in the next section. Fig. 3(b) and (d) show the two spline contours on the OCT images with NIH.

2.3 Stent Strut Detection

Looking at a typical OCT frame with stents (Figure 4-a), it is easy to observe that stent struts usually block the penetration of the infrared light and leave a dark shadow in the

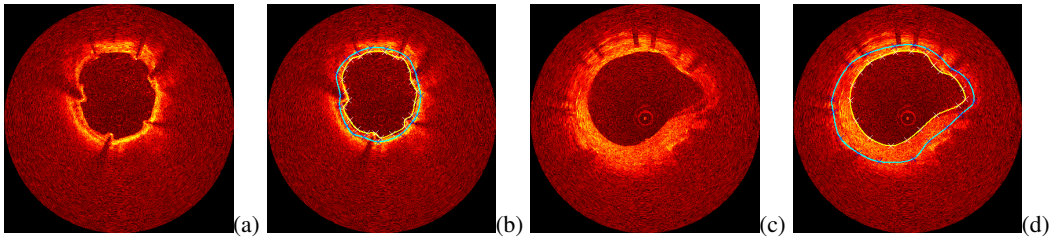

Fig. 3. (a) an OCT image frame with minimum NIH; (b) Spline is deformed over the image (a) to fit to the strut boundary; (c) an OCT image frame with extreme NIH; (d) Spline is deformed the over image (c) to fit to the strut boundary.

far field of the image domain. We developed a stent strut detection algorithm based on the shadows by shooting imaginary rays from the center of the catheter to imitate the real light beams. Traversing the rows of the rectangular OCT image data, and starting from the spline contour $\boldsymbol{C}$ on each row, we sample the intensity profile towards the far field to form the energy:

$$E(y) = \int_{\boldsymbol{C}(y,x)}^{\boldsymbol{C}(y,x+r)} I(x)dx$$

This forms a vector of estimated energies in the vicinity of the lumen contour in its normal direction, which coincides with the infrared beam direction. Here, r, which is the extent of the energy interval, is a certain percentage set intuitively and heuristically, e.g. 10% of the range size M (column size) of the rectangular image.

Next, to detect possible shadows of struts, using the normal energy, the contour is traversed tangentially. The energy $E(y)$'s are differentiated to detect the start and end of the strut shadows. Hence, the following rules are obtained:

$$\text{Strut} = \{ \begin{array}{ll} \text{strut shadow start} & \textit{if } \nabla \text{E}^{-}(y) < S\% \\ \text{strut shadow end} & \textit{if } \nabla \text{E}^{+}(y) < S\% \end{array} \tag{7}$$

where the ∇^{-} and ∇^{+} indicate discrete approximations to one-sided derivatives of E on each side of the current coordinate y, normalized to (0,1), and S is a percentage that signifies the drop in the energy of the intensity, hence the strut shadow. The parameter S was set to 80%.

Even if the struts are narrow and have vague trailing shadows, our strategy of traversing the image both in radial and tangential vessel wall direction and integrating the intensities helps improve the robustness. Our shadow detection algorithm works for most cases when there are reasonably defined trailing shadows of struts, as shown in Figure 4. In the figures, the circles depict the struts that are detected by our algorithm with their radii indicating the width of the shadow, hence an approximation to the strut width. As can be seen from images in (c)-(f), starting from the second spline contour, our algorithm is able to detect struts in the more challenging NIH imaging scenarios as well.

Sew-up stitch problem in the Pullbacks: A typical artifact, called as the sew-up stitch, is observed in Figure 5.a at 8 o'clock. During a pullback operation, the catheter is moving while sending the light beam sideways to image the vessel wall. As the full 360^{o} rotation

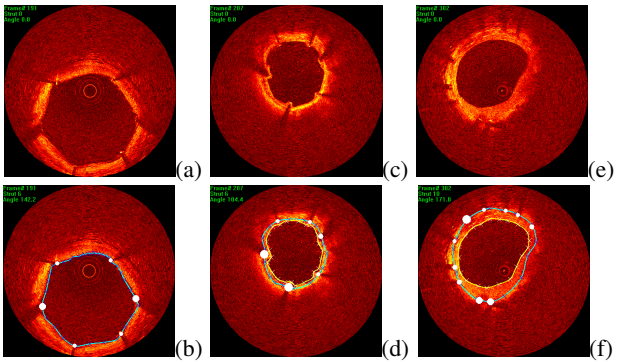

Fig. 4. (a) an OCT image frame with newly implanted stents; (b) detected struts ; (c) image with minimum NIH case; (d) detected struts over the second spline; (e) image with extreme NIH case; (f) detected struts over the second spline.

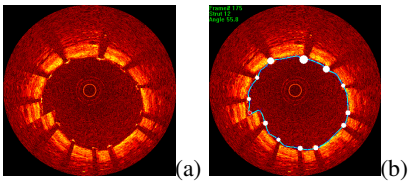

Fig. 5. (a) an OCT image frame with sew-up stitching problem; (b) Detected and marked with a red circle.

is completed for recording one cross-section image, the catheter has already advanced slightly in physical space in $1/15^{th}$ of a second during a catheter pullback at 1mm/s, therefore, the 0^o and 360^o beams do not end up at the same position, and the sew-up stitches appear as easily observed as a seaming artifact in the display image. Our strut detection method will sometimes label these artifacts as struts when they leave shadow-like trails. Therefore, we detect this situation by computing the tangent of the spline on the rectangular image, and the persistence of the orientation of the tangent vector to stay roughly horizontal (i.e. $\pm 10^o$) for a few positions on the contour. Figure 5.b shows an example detection of the stitch region and it is marked with a red circle and later removed from the strut list.

3 Results

Our data set consisted of 20 *in vivo* OCT pullbacks of each several hundred image frames, with raw rectangular image size of $N \times M = 200 \times 700$. The pullback images were acquired with a LightLab OCT transducer and the pullback speed was $1mm/s$ with an axial resolution of 12 microns. Parameters in our algorithm are fixed as follows. The density mode parameter b in the prefiltering step, is set to 15%. The "minimum width threshold" in the spline initialization step is set to 20% of the rectangular image column M. For the spline motion equation Eq 6, the weight $w_1 = 1$, and $w_2 = 0.1$. Our method is robust against the parameter set, and once set, they were not changed during the experiments.

Our algorithm works in near real time, which takes less than 1 second to complete the spline segmentation and strut detection, therefore can be used interactively online.

For our validation studies, we compared manual strut detection with automatic detection over a set of images. The expert interventional cardiologist in our team, went through 7 of the OCT pullbacks and tested our method over a total of 33 images. Among these seven pullbacks, three of them had newly implanted stents, three had minimum NIH in the stents (DES), and one had much more NIH (BMS) over stents. For the assessment of

Cases	% correctly detected number of struts	Max Angle btw struts	Stent Eccentricity
New Implant	0.86 ± 0.12	59.6 ± 15.4	0.73 ± 0.08
NIH Cases	0.86 ± 0.09	77.5 ± 21.3	0.67 ± 0.11
All cases	0.86 ± 0.10	71.3 ± 21.1	0.69 ± 0.10

Table 1. Validation Studies: Normalized number of detected struts, maximum angle between struts, stent eccentricity are calculated over our dataset with newly implanted stent cases and neointimal tissue growth cases.

strut distribution, on each image frame, we measure the total number of detected struts, the strut eccentricity, and the maximum angle between the struts as shown in Table 1 as the mean$\pm$standard deviation values. The percentage of correctly detected struts is calculated over each image as $1 -$ normalized error where the normalized error is defined as the absolute difference between the number of struts marked by the physician and the number of struts detected by our algorithm, which is later normalized by the physician marked strut count. In these first set of validation studies, our algorithm achieved a reasonably good accuracy in detection, which is around 86%.

One interesting parameter to assess is the maximum angle between struts in a frame. Looking from a circular distribution point of view, if one half of the stent circumference has less struts than the other, this may be an indicator for less drug presence hence more NIH on that side of the vessel wall.

Another measure we calculated is the stent eccentricity, defined as the minimum divided by the maximum stent diameter calculated by our algorithm. This is another indicator for malpositioning of the stent as can be observed in the last column of Table 1 farther away from 1, the ideal eccentricity.

Finally, the computer application we have developed is aimed at clinical use, therefore, we have included interaction components such as possibility of correcting the spline contours, and marking the struts that are misdetected. To distinguish between the different phases after stent implant, mode of operation is easily chosen to indicate that the OCT pullback has a newly implanted stent or an NIH case, so that in the latter case a second spline contour can be estimated or drawn by the user.

4 Conclusions and Discussions

We presented novel computational methods for automatic stent implant follow-up from OCT pullbacks. We developed a new spline-based segmentation method for both the lumen boundary and stent strut boundaries. Following that, we described a strut detection

algorithm by detecting their trailing shadows in the OCT images, which is to the best of our knowledge new in the computational medical imaging. In the end, a strut distribution analysis is carried out and a number of measures important for stent implant follow-up and monitoring of the neointimal tissue growth over struts are calculated. Our experimental results demonstrated that our algorithm works well on the segmentation of target boundaries in OCT images, and detected stent struts and their trailing shadows in presence. In most cases, the shadow that corresponds to a stent strut is visible and detectable, but sometimes there are struts whose trailing shadows are not visible. Our ongoing work to improve our method includes a second pass to follow the contour and detect the visible bright struts, which were missed with the shadow detection only.

Our results and initial validation tests are very promising, however, further extensive validation studies will be performed to test and improve our stent follow-up analysis system. Our algorithm provides a convenient tool that automatically detects and analyzes the distribution of stent struts, thus reduces a lot of manual work that is associated with this task and thus will be a useful computer-aided monitoring tool in the procedure of stent implantation and its follow-up studies.

References

1. Brezinski, M.E., Tearney, G.J., Brett, B.E.: Imaging of coronary artery microstructure with optical coherence tomography. "American Journal of Cardiology" **77** (1996) 92–93
2. Jang, I., Bouma, B., Kang, D., Park, S., Park, S., Seung, K., Choi, K., Shishkov, M., Schlendorf, K., Pomerantsev, E., Houser, S., Aretz, H., Tearney, G.: Visualization of coronary atherosclerotic plaques in patients using optical coherence tomography: Comparison with intravascular ultrasound. "American Journal of Cardiology" **39** (2002) 604–609
3. Patwari, P., Weissman, N.J., Boppart, S.A., Jesser, C., Stamper, D., Fujimoto, J.G., Brezinski, M.E.: Assessment of coronary plaque with optical coherence tomography and high-frequency ultrasound. "American Journal of Cardiology" **85** (2000) 641–644
4. Yabushita, H., Bouma, B., Houser, S., Aretz, H., Jang, I.K., Schlendorf, K., Kauffman, C., Shishkov, M., Kang, D.H., Halpern, E., Tearney, G.: Characterization of human atherosclerosis by optical coherence tomography. "Circulation" **106** (2002) 1640–1645
5. Xu, C., Schmitt, J., Carlier, S., Virmani, R.: Characterization of atherosclerosis plaques by measuring both backscattering and attenuation coefficients in optical coherence tomography. "Journal of Biomedical Optics" **13**(3) (2008)
6. Sousa, J., Costa, M., Sousa, A., Abizaid, A., Seixas, A., Abizaid, A., Feres, F., Mattos, L., Falotico, R., Jaeger, J., Popma, J., Serruys, P.: Two-year angiographic and intravascular ultrasound follow-up after implantation of sirolimus-eluting stents in human coronary arteries. "Circulation" **107** (2003) 381–383
7. Lemos, P., Saia, F., Ligthart, J., Arampatzis, C., Sianos, G., Tanabe, K., Hoye, A., Degertekin, M., Daemen, J., McFadden, E., Hofma, S., Smits, P., de Feyter, P., van der Giessen, W., van Domburg, R., Serruys, P.: Coronary restenosis after sirolimus-eluting stent implantation: morphological description and mechanistic analysis from a consecutive series of cases. "Circulation" **108** (2003) 257–260
8. Hwang, C.W., Wu, D., Edelman, E.R.: Physiological transport forces govern drug distribution for stent-based delivery. "Circulation" **104** (2001) 600–605
9. Takebayashi, H., Mintz, G., Carlier, S., Kobayashi, Y., Fujii, K., T.Yasuda, Costa, R., Moussa, I., Dangas, G., Mehran, R., Lansky, A., Kreps, E., Collins, M., Colombo, A., Stone, G., Leon, M., Moses, J.: Nonuniform strut distribution correlates with more neointimal hyperplasia after sirolimus-eluting stent implantation. "Circulation" **110** (2004) 3430–3434

10. Dijkstra, J., Koning, G., Tuinenburg, J., Oemrawsingh, P., Reiber, J.: Automatic stent border detection in intravascular ultrasound images. In: Proceedings of CARS. (2003) 1111–1116
11. Kass, M., Witkin, A., Terzopoulos, D.: Snakes: Active contour models. Int. J. Computer Vision **1**(4) (January 1988) 321–331
12. Unal, G., Bucher, S., Carlier, S., Slabaugh, G., Fang, T., Tanaka, K.: Shape-driven segmentation of the arterial wall intravascular ultrasound images. IEEE Trans. Information Technology in Biomedicine **12**(3) (2008) 335–347
13. Caselles, V., Kimmel, R., Sapiro, G.: Geodesic active contours. In: ICCV95. (1995) 694–699
14. Kichenassamy, S., Kumar, A., Olver, P., Tannenbaum, A., Yezzi, A.: Gradient flows and geometric active contours. In: Proc. ICCV. (1995) 810–815
15. Slabaugh, G., Kong, K., Unal, G., Fang, T.: Variational guidewire tracking using phase congruency. In: MICCAI, LNCS 4792, Brisbane, Australia, Springer (2007) 612–619
16. van Dam Foley, J., Feiner, S., Hughes, J.: Computer Graphics: Principles and Practice. 2nd edn. Addison Wesley Reading (1996)
17. Catmull, E., Rom, R.: A class of local interpolating splines. In Barnhill, R.E., Reisenfeld, R.F., eds.: Computer Aided Geometric Design, Academic Press, New York (1974) 317–326